Infrared Excess sources: Compton thick QSOs, low-luminosity Seyferts or starbursts?

A. Georgakakis,[1]⋆ M. Rowan-Robinson,[2] K. Nandra,[2] J. Digby-North[2]
P. G. Pérez-González[3,4] and G. Barro[3]

[1]*National Observatory of Athens, V. Paulou & I. Metaxa, 11532, Greece*

[2]*Astrophysics Group, Blackett Laboratory, Imperial College, Prince Consort Rd, London SW7 2AZ*

[3]*Departamento de Astrofísica, Facultad de CC. Físicas, Universidad Complutense de Madrid, E-28040 Madrid, Spain*

[4]*Department of Astronomy, Steward Observatory, 933 North Cherry Avenue, Tucson, AZ 85721-0065, USA*

ABSTRACT

We explore the nature of Infrared Excess sources (IRX), which are proposed as candidates for luminous [$L_X(2–10\,\mathrm{keV}) > 10^{43}\,\mathrm{erg\,s^{-1}}$] Compton thick ($N_H > 2 \times 10^{24}\,\mathrm{cm^{-2}}$) QSOs at $z \approx 2$. Lower redshift, $z \approx 1$, analogues of the distant IRX population are identified by first redshifting to $z = 2$ the spectral energy distributions (SEDs) of all sources with secure spectroscopic redshifts in the AEGIS (6488) and the GOODS-North (1784) surveys and then selecting those that qualify as IRX sources at that redshift. A total of 19 galaxies are selected. The mean redshift of the sample is $z \approx 1$. We do not find strong evidence for Compton thick QSOs in the sample. For nine sources with X-ray counterparts, the X-ray spectra are consistent with Compton thin active galactic nucleus (AGN). Only three of them show tentative evidence for Compton thick obscuration. The SEDs of the X-ray undetected population are consistent with starburst activity. There is no evidence for a hot dust component at the mid-infrared associated with AGN heated dust. If the X-ray undetected sources host AGN, an upper limit of $L_X(2–10\,\mathrm{keV}) = 10^{43}\,\mathrm{erg\,s^{-1}}$ is estimated for their intrinsic luminosity. We propose that a large fraction of the $z \approx 2$ IRX population is not Compton thick quasi-stellar objects (QSOs) but low-luminosity [$L_X(2–10\,\mathrm{keV}) < 10^{43}\,\mathrm{erg\,s^{-1}}$], possibly Compton thin, AGN or dusty starbursts. It is shown that the decomposition of the AGN and starburst contribution to the mid-IR is essential for interpreting the nature of this population, as star formation may dominate this wavelength regime.

Key words: surveys – galaxies: active – galaxies: Seyfert – galaxies: starburst.

1 INTRODUCTION

The composition of the diffuse X-ray background remains a problem for high-energy astrophysics. X-ray imaging surveys with the Chandra and *XMM–Newton* observatories have resolved between 80 and 100 per cent of the XRB into discrete sources below about 6 keV (e.g. Worsley et al. 2005; Hickox & Markevitch 2006; Georgakakis et al. 2008). The vast majority of these sources are Compton thin active galactic nucleus (AGN) ($N_H \lesssim 10^{24}\,\mathrm{cm^{-2}}$) at a mean redshift $z \approx 1$ (e.g. Barger et al. 2005; Akylas et al. 2006). At higher energies however, between 20 and 30 keV, where the bulk of the XRB energy is emitted (Marshall et al. 1980), only a small fraction of its total intensity has been resolved into discreet sources (Sazonov et al. 2007). As a result, the nature of the populations that

make up the XRB at these energies is still not well known. Population synthesis models use our knowledge on the properties of the X-ray sources below ≈10 keV to make predictions on the nature of the X-ray populations close to the peak of the XRB (e.g. Gilli, Comastri & Hasinger 2007). These models indicate that Compton thin AGN alone cannot account for the shape of the XRB spectrum at ≈20–30 keV. An additional population of heavily obscured, Compton thick ($N_H \gtrsim 10^{24}\,\mathrm{cm^{-2}}$) AGN is postulated to reconcile the discrepancy (e.g. Gilli et al. 2007). The required number density of such sources is, however, under debate (Draper & Ballantyne 2009; Treister, Urry & Virani 2009b). Unfortunately, the identification of the heavily obscured AGN population predicted by the models is far from trivial. The X-ray emission of these sources below about 10 keV is suppressed by photoelectric absorption and as a result most of them are expected to lie well below the sensitivity limits of the deepest current X-ray observations. Although a handful of Compton thick AGN candidates have been identified in deep X-ray

⋆E-mail: age@astro.noa.gr

surveys (Tozzi et al. 2006; Georgantopoulos et al. 2009), the bulk of this population remains to be discovered.

Selection at the mid-IR (3–30 μm) is proposed as a powerful tool for finding heavily obscured X-ray faint AGN. The UV/optical photons emitted by the central engine are absorbed by the gas and dust clouds and appear as thermal radiation with a broad bump in the mid-IR (νf_ν units; e.g. Elvis et al. 1994; Prieto et al. 2010). Diverse selection methods have been developed to identify this AGN spectral signature in the mid-infrared. Lacy et al. (2004), Stern et al. (2005) and Hatziminaoglou et al. (2005) propose simple colour cuts based on the mid-IR colours of luminous high-redshift quasi-stellar objects (QSOs) and/or type-2 Seyferts. Polletta et al. (2006) and Rowan-Robinson, Valtchanov & Nandra (2009) fit templates to the broad-band photometry from UV to the far-IR. Alonso-Herrero et al. (2006) and Donley et al. (2007) select sources with power-law spectral energy distributions (SEDs) in the mid-IR. The methods above have merits and shortcomings. Selection by mid-IR colour, for example, is simple but suffers contamination from star-forming galaxies if applied to the deepest mid-IR samples currently available (Donley et al. 2008; Georgantopoulos et al. 2008). Template fits are powerful but require high-quality photometry over a wide-wavelength baseline for meaningful constraints. Power-law SEDs provide the most clean samples of infrared-selected AGN, but are sensitive only to the most luminous and hence, rare sources.

A much promising method that is believed to be efficient in identifying heavily obscured, possibly Compton thick, AGN is based on the selection of sources that are faint at optical and bright at mid-IR wavelengths. In its simplest version this method applies a cut in the 24 μm over R-band flux density ratio, $f_{24\,\mu m}/f_R > 1000$ to identify dust obscured galaxies (DOGs; Dey et al. 2008) at a mean redshift $z \approx 2$. In addition to the limit above, Fiore et al. (2008, 2009) also use the colour cut $R - K > 4.5$ to select Infrared-Excess sources (IRXs). This colour selection is motivated by the observational result that redder sources include a higher fraction of obscured AGN (e.g. Brusa et al. 2005). A different approach has been adopted by Daddi et al. (2007). They select BzK sources that show excess mid-IR emission relative to that expected based on the rates of star formation measured from shorter wavelengths. Despite differences in the adopted criteria, all the studies above identify a population of galaxies with similar properties in terms of average redshift ($z \approx 2$), mean X-ray properties and mid-IR luminosities. These sources are believed to be massive galaxies ($M_{\mathrm{star}} \approx 10^{10}$–$10^{11}\,M_\odot$, Treister et al. 2009; Bussmann et al. 2009a) that experience intense bursts of star formation and rapid supermassive black hole growth, possibly triggered by mergers (e.g. Bussmann et al. 2009a; Narayanan et al. 2009). The apparently brighter subset of this population ($S_{24} > 300\,\mu$Jy) are proposed as descendants of Submillimeter Galaxies on their way to becoming unobscured QSOs (e.g. Bussmann et al. 2009a,b; Narayanan et al. 2009), which will eventually evolve into present-day $4\,L^*$ galaxies (Dey et al. 2008; Brodwin et al. 2008). Although these sources are undoubtedly important for understanding the co-evolution of galaxies and SBHs at high redshift, in this paper we focus on their significance to XRB studies by putting into test claims that they include a large fraction of Compton thick AGN. The two key properties of these sources (hereafter referred to as IRX sources), which are interpreted as evidence for Compton thick AGN are (i) their hard mean X-ray spectrum and (ii) their faintness at X-ray wavelengths relative to the mid-IR. The first point is demonstrated in Fig. 1 which shows the that the mean hardness ratio of the IRX sources is consistent with that of the local Compton thick AGN NGC 1068 (Matt et al. 1999). With respect to the second point, the major-
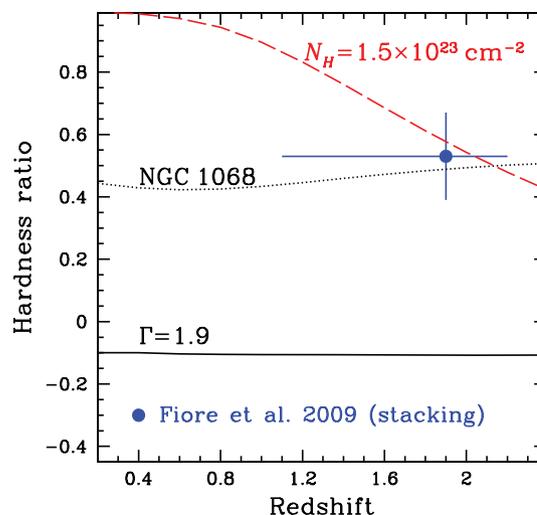

Figure 1. Hardness ratio against redshift. The hardness ratio is defined as HR=(H−S)/(H+S), where H and S are the counts in the 1.5–6 and 0.3–1.5 keV energy intervals, respectively. The (blue) dot is the mean hardness ratio of X-ray undetected sources in the COSMOS survey (Fiore et al. 2009) estimated using stacking analysis. The vertical error bar is the 1σ uncertainty of the HR, while the horizontal error bar shows the redshift range of the Fiore et al. (2009) IRX population. The dotted line (black) shows the expected HR of the local Compton thick AGN NGC 1068 (Matt et al. 1999). The (red) dashed curve corresponds to the HR of a power-law X-ray spectrum with photon index $\Gamma = 1.9$, which is absorbed by a column density of $N_H = 1.5 \times 10^{23}\,\mathrm{cm}^{-2}$. The continuous (black) line corresponds to the HR of an unobscured AGN, i.e a power-law X-ray spectrum with photon index $\Gamma = 1.9$.

ity of the IRX sources (80 per cent; Georgantopoulos et al. 2008) are not detected in the deepest X-ray surveys available and their mean X-ray properties can only be studied through stacking analysis. Fig. 2 shows the average X-ray-to-mid-IR luminosity ratio, $L_X(2$–$10\,\mathrm{keV})/\nu L_\nu 5.8\,\mu$m, of the X-ray undetected IRX population. Relative to local AGN from the sample of Lutz et al. (2004) these sources appear underluminous in the mid-IR by 2–3 dex. Assuming a narrow range of $L_X(2$–$10\,\mathrm{keV})/\nu L_\nu 5.8\,\mu$m for typical AGN (e.g. Lutz et al. 2004), the position of the IRX population in Fig. 2 is consistent with a Compton thick obscuring screen that suppresses the observed X-ray emission relative to the mid-IR. Under the assumption that the mid-IR luminosity is a good proxy of the AGN power, one can estimate intrinsic 2–10 keV luminosities for the IRX sources in excess of $10^{43}\,\mathrm{erg\,s}^{-1}$ (Daddi et al. 2007; Fiore et al. 2008, 2009; Treister et al. 2009). AGN with intrinsic luminosities above this limit are hereafter referred to as QSOs. IRX sources are therefore excellent candidates for the Compton thick QSOs needed by population synthesis models to explain the XRB spectrum at 20–30 keV. Simulations indeed show that the bulk of these sources (80 per cent, Fiore et al. 2008; 95 per cent, Fiore et al. 2009) are likely to be Compton thick QSOs, while their estimated space densities are consistent with the predictions of the XRB models.

Although there is no doubt that the IRX population includes a fraction of heavily obscured AGN (Georgantopoulos et al. 2009), the evidence for Compton thick sources is far from conclusive. The two key properties of the IRX sources, hardness ratio and X-ray-to-mid-IR luminosity ratio, are also consistent with Compton thin AGN of lower luminosity, hereafter defined as $L_X(2$–$10\,\mathrm{keV}) < 10^{43}\,\mathrm{erg\,s}^{-1}$. Fig. 1, for example, shows that the mean hardness ratio of this population could be due to moderate obscuring column
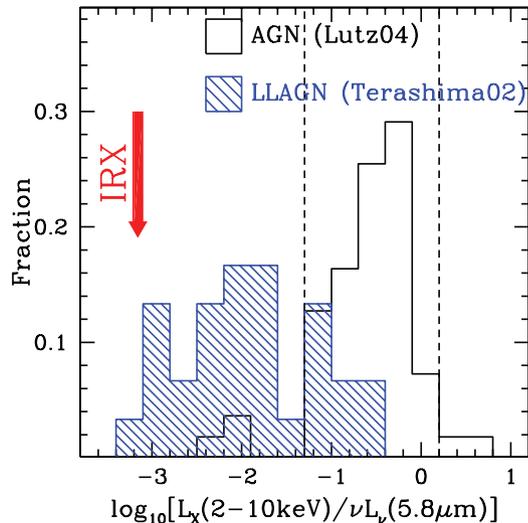
Figure 2. Distribution of X-ray–to–mid-IR luminosity ratio, $L_X(2\text{–}10\,\text{keV})/\nu L_\nu(5.8\,\mu\text{m})$. The (black) unshaded histogram is for AGN from Lutz et al. (2004). This sample was selected to include only AGN that dominate in the mid-IR. The vertical dashed lines show the dispersion of the X-ray–to–mid-IR luminosity ratio for the same sample. The low-luminosity AGN of Terashima et al. (2002) are shown with the blue hatched histogram. The mean $L_X(2\text{–}10\,\text{keV})/\nu L_\nu(5.8\,\mu\text{m})$ of IRX sources is plotted with the (red) arrow. This estimate is for X-ray undetected IRX sources in the CDF-North (Georgantopoulos et al. 2008). The mean X-ray luminosity of this population is determined via stacking analysis and $\nu L_\nu(5.8\,\mu\text{m})$ is the average mid-IR luminosity of the sample. Both luminosities are estimated assuming $z = 2$ for the IRX sources. The 5.8 μm luminosity of the Terashima et al. (2002) sources is determined using the IRAS 12 μm flux density and adopting an average flux density ratio $f_{12\,\mu\text{m}}/f_{5.8\,\mu\text{m}} = 0.9$, estimated from the subsample of these sources with 6 μm flux density measurements from the literature. The 2–10 keV X-ray luminosities of the Terashima et al. (2002) AGN are corrected for obscuration, except for a total of six sources in that sample, which show a strong Fe Kα 6.4 keV line in their X-ray spectra with equivalent width $EW > 900$ eV and are therefore Compton thick candidates.

densities of few times $10^{23}\,\text{cm}^{-2}$. Moreover, Fig. 2 demonstrates that lower-luminosity Compton thin AGN (Terashima et al. 2002) have very low X-ray-to-mid-IR luminosity ratios, i.e. similar to those observed for IRX sources. This is not surprising as both AGN and star formation contribute to the mid-IR, thereby resulting in a broad $L_X(2\text{–}10\,\text{keV})/\nu L_\nu 5.8\,\mu\text{m}$ distribution. One has to isolate the AGN component at the mid-IR part of the SED to get a tight correlation with X-ray luminosity (e.g. Prieto et al. 2010). Lutz et al. (2004), for example, accomplished that by selecting *only* sources where the AGN dominates in the mid-IR, i.e. those *without* a significant starburst component relative to the AGN. For the high-redshift IRX sources it is not clear what fraction of the mid-IR emission is from AGN heated dust. Only under the strong assumption that the *bulk* of the mid-IR luminosity is associated with reprocessed radiation from accretion on the central SBH, can one infer that these sources are Compton thick QSOs. A number of studies on the IRX sources have already suggested that this population may include a large fraction of lower-luminosity Compton thin AGN or even dusty starbursts (e.g. Georgantopoulos et al. 2008; Donley et al. 2008; Pope et al. 2008; Murphy et al. 2009).

Elucidating the nature of IRX sources, Compton thick QSOs, Compton thin lower-luminosity AGN or starbursts, requires very deep X-ray data and/or AGN/starburst decomposition at the mid-IR. Unfortunately, IRX samples at $z \approx 2$ are too faint at almost

any wavelength, expect the mid-IR, for such a detailed study. In this paper we address this issue by selecting lower-redshift ($z \approx 1$) analogues of the distant ($z \approx 2$) IRX population. The advantage of this approach is that the selected sources are apparently bright and therefore their SEDs can be constrained over a wide wavelength baseline, from the far-UV to the far-IR. The sources are selected in fields with some of the deepest X-ray observations available (Chandra Deep Field North, All wavelength Extended Groth strip International Survey: AEGIS), thereby allowing study of their X-ray properties via spectral analysis. An additional advantage of our strategy is that there is only about 2.5 Gyr difference in the age of the Universe between $z = 1$ and $z = 2$ ($H_0 = 70\,\text{km s}^{-1}\,\text{Mpc}^{-1}$, $\Omega_M = 0.3$, $\Omega_\Lambda = 0.7$). Therefore, by selecting galaxies at $z \approx 1$, it is more likely to identify systems that are physically similar to the IRX population at ≈ 2. In this respect it is interesting that in the local Universe there are no known analogues of the IRX sources, which can be used to study in detail the nature of this population (e.g. Dey et al. 2008).

Throughout this paper we adopt $H_0 = 70\,\text{km s}^{-1}\,\text{Mpc}^{-1}$, $\Omega_M = 0.3$ and $\Omega_\Lambda = 0.7$.

2 DATA

The UV to far-IR data used in this study are from the Universidad Complutense de Madrid (UCM) Cosmological Surveys Data base,[1] which combines all the photometric and spectroscopic observations available in prime cosmological survey fields. Details on the data reduction, band merging and photometry are presented by Pérez-González et al. (2005, 2008). The fields of choice for this paper are the AEGIS and GOODS-North. In both fields the IRAC 3.6 μm selected catalogues are used, which reach limiting magnitudes (AB system) of $[3.6] = 25.5$ and 24.5 mag, respectively. A total of 80 237 and 9061 sources are detected in the AEGIS and GOODS-North, respectively, to the limits above.

The multiwavelength data in AEGIS include (i) photometry in the GALEX far- and near-ultraviolet wavebands (FUV and NUV, respectively; Davis et al. 2007); (ii) *BRI* observations from the Canada–France–Hawaii Telescope CFHT12K mosaic camera (Coil et al. 2004); (iii) *ugriz* imaging from the T0003 data release of the Canada–France–Hawaii Telescope Legacy Survey (CFHTLS; Ilbert et al. 2006); (iv) *Spitzer* IRAC observations at 3.6, 4.5, 5.8 and 8.9 μm (Barmby et al. 2008) obtained as part of the Guaranteed Time Observing (GTO) programme and (v) *Spitzer* MIPS photometry at 24 and 70 μm by co-adding GTO data with the second data release of the Far-Infrared Deep Extragalactic Legacy Survey (FIDEL). Spectroscopy in the AEGIS is primarily from the DEEP2 survey (Davis et al. 2003, 2007) and a number of smaller spectroscopic programmes that targeted the original Groth Strip (Weiner et al. 2005, and references therein).

The photometry in the GOODS-North includes (i) GALEX FUV and NUV data, (ii) deep *UBVRIz* ground based imaging presented by Capak et al. (2004), (iii) *Spitzer* IRAC (3.6, 4.5, 5.8 and 8.9 μm) and MIPS 24 μm observations obtained as part of the GOODS programme, MIPS 70-μm data from FIDEL. Optical spectroscopy in the GOODS-North is available either from programmes that specifically target the X-ray population in this field (e.g. Barger et al. 2003, 2005; Cowie et al. 2003) or from the Keck Treasury Redshift Survey (TKRS; Wirth et al. 2004).

---

[1] http://guaix.fis.ucm.es/~pgperez

The X-ray observations of the Extended Groth Strip (AEGIS-X) consist of eight ACIS-I (Advanced CCD Imaging Spectrometer) pointings, each with a total integration time of about 200 ks split in at least three shorter exposures obtained at different epochs. The GOODS-North lies in central and most sensitive region of the Chandra Deep Field North (CDF-N) survey, which consists of 20 individual ACIS-I observations, which sum up to a total exposure time of 2 Ms. The CDF-N and AEGIS-X data reduction, source detection and flux estimation have been carried out in a homogeneous way using the methodology described by Laird et al. (2009).[2] Sources with Poisson probabilities $<4 \times 10^{-6}$ are detected in four energy bands: full (0.5–7 keV), soft (0.5–2 keV), hard (2–7 keV) and ultra-hard (5–7 keV). The count rates in the above energy intervals are converted to fluxes in the standard bands 0.5–10, 0.5–2, 2–10 and 5–10 keV, respectively, assuming a power-law X-ray spectrum with $\Gamma = 1.4$ absorbed by the Galactic hydrogen column density appropriate for each field. The 2–10 keV fluxes where the sensitivity curves drop to half their maxima are 2×10^{-14} and 2×10^{-16} erg s^{-1} cm^{-2} for the AEGIS-X and CDF-N surveys, respectively. The identification of the X-ray sample with the IRAC 3.6-μm sources has been carried out using the The Likelihood Ratio method (LR; Sutherland & Saunders 1992; Laird et al. 2009; Georgakakis et al. 2009). In the AEGIS, of the 918 X-ray sources that overlap with the *Spitzer* IRAC survey region, 867 (93 per cent) have an IRAC counterpart with likelihood $LR > 0.5$ and an estimated contamination rate of 1.5 per cent. In the CDF-North 335 X-ray sources overlap with the GOODS-North IRAC data, of which 301 (90 per cent) have counterparts with $LR > 0.5$. The expected contamination rate is about 1.4 per cent.

3 SAMPLE SELECTION

Lower redshift analogues of the $z \approx 2$ IRX population are identified as follows. First, IRAC 3.6-μm sources with spectroscopic redshifts only are selected. When a spectroscopic quality flag is available, we select sources with redshift determinations secure at the >90 per cent confidence level (i.e. quality flag $Q \geq 3$ for the DEEP2 and the TKRS surveys). This reduces the sample to 1784 sources in the GOODS-North and 6488 the AEGIS. This is to avoid uncertainties in the determination of the rest-frame SEDs associated with insecure spectroscopic redshift determinations or photometric redshift errors. The rest-frame SEDs of the spectroscopically identified IRAC 3.6-μm sources are then redshifted to $z = 2$, the mean redshift of the IRX population. We select only those sources which at $z = 2$ have *observed* SEDs with $f_{24\,\mu m}/f_R > 900$ and $R - [3.6] > 3.7$ mag (AB system), i.e. similar to the criteria used by Fiore et al. (2008, 2009) to define their IRX sample. Georgantopoulos et al. (2008) have shown that the colour cut $R - [3.6] > 3.7$ mag adopted here is similar to the $R - K > 4.5$ mag used by Fiore et al. (2008, 2009). The method for selecting lower redshift analogues of the $z \approx 2$ IRX population is demonstrated by the dotted lines in Fig. 3, which plots the flux density ratio $f_{24\,\mu m}/f_R$ against $R - [3.6]$ colour. A total of 19 sources (14 in the AEGIS and five in the GOODS-North) are selected. The sample is presented in Table 1. The observed flux densities of the sources are shown in Table 2 for the AEGIS and Table 3 for the GOODS-North galaxies.

For the estimation of the $z = 2$ SED, we interpolate linearly between observed data points. It is recognized that the mid-IR is a
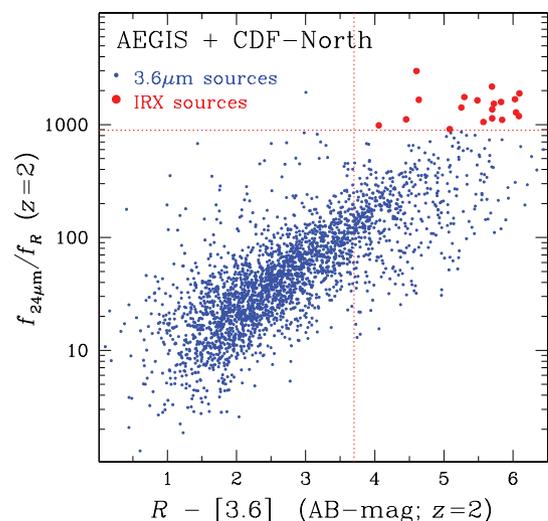
Figure 3. $f_{24\,\mu m}/f_R$ against $R - [3.6]$ estimated by redshifting to $z = 2$ the rest-frame SEDs of 3.6 μm sources in the AEGIS and the CDF-North with spectroscopic redshifts (blue dots). Large red circles are the subset of those sources which at $z = 2$ have $f_{24\,\mu m}/f_R > 900$ and $R - [3.6] > 3.7$ mag (dotted horizontal and vertical lines, respectively), i.e. similar to the IRX source selection criteria (Fiore et al. 2008, 2009; Georgantopoulos et al. 2008).

complex wavelength regime with PAHs and/or the silicate absorption/emission feature at 9.7 μm having a strong impact on the observed broad-band flux densities. The linear interpolation approach is ignoring these subtleties but is preferred over more complex template fitting schemes as it is model independent. It is confirmed nevertheless, that the sources presented in Table 1 satisfy the IRX criteria at $z = 2$ if the SED fits described in Section 4 are used to interpolate between data points. The *Spitzer* MIPS 24 μm waveband and the *R*-band correspond to rest-frame wavelengths of about 8 and 0.22 μm at $z = 2$, respectively. In order to avoid uncertain extrapolations of the SED, we only consider sources with flux density detections, *not* upper limits, at rest-frame wavelengths shorter than 0.22 μm and longer than 8 μm. In practice this means that for the typical redshift of the sources in the sample, they should be detected at 24 μm or longer wavelengths and the *U*-band or shorter wavelengths. Three sources in the AEGIS are not detected at 24 μm and therefore the observed 24-μm flux density at $z = 2$ is estimated by interpolating the SED between 8 and 70 μm.

We caution that the sample of IRX sources selected in this paper is by no means complete. For example, the requirement for secure spectroscopic redshifts translates to an optical magnitude limit of $R \approx 24$ mag. It can be shown, however, that this does not introduce a bias to the sample, i.e. in favour of optically bright sources. We calculate that the median *observed* *R*-band flux density of our sources if they were at $z = 2$ would be ≈ 0.04 μJy. This is estimated after scaling with the appropriate *k*-corrections (i.e. $1 + z$ factor) and luminosity distances the *B*-band flux densities of our sources, which roughly correspond to the *R*-band at $z = 2$. The number above should be compared with the median *R*-band flux density of ≈ 0.07 μJy for sources in the AEGIS and the GOODS-North fields with observed $f_{24\,\mu m}/f_R > 900$ and $R - [3.6] > 3.7$ mag (AB system). If anything our sample is sensitive to somewhat optically fainter sources compared to the $z \approx 2$ IRX population in the AEGIS and the GOODS-North fields. Additionally, the median 5.8 μm luminosity of our IRX sample, is $\nu L_\nu(5.8\,\mu m) \approx 1.6 \times 10^{44}$ erg s^{-1}, about two times fainter than the median 5.8 μm luminosity of the

Table 1. Sample.

ID	RA (J2000)	Dec. (J2000)	z	$f_{24\,\mu m}/f_R$ (z = 2)	$R - [3.6]$ (z = 2)	$\log L_{sb}$ (L$_\odot$)	$\log L_{tor}$ (L$_\odot$)	type	A_V (mag)	$\log$ SFR (M$_\odot$ yr^{-1})
irx-1	14 16 17.37	+52 12 38.25	0.6826	2172	5.7	11.37	–	E	–	1.67
irx-2	14 16 32.79	+52 19 01.94	1.0284	984	4.1	11.62	11.62	QSO	0.8	1.92
irx-3	14 16 21.80	+52 20 06.35	0.7602	1587	5.8	11.39	–	E	–	1.69
irx-4	14 16 18.74	+52 23 19.24	0.8360	1188	6.1	11.40	–	E	–	1.70
irx-5	14 16 50.49	+52 16 35.11	0.6829	1678	6.0	10.87	10.57	E	–	1.17
irx-6	14 16 51.00	+52 23 17.68	1.0246	1103	5.8	11.42	–	E	–	1.72
irx-7	14 17 23.10	+52 27 49.57	0.9024	1891	6.1	11.41	–	E	–	1.71
irx-8	14 17 41.87	+52 28 23.42	1.1482	1753	5.3	12.34	12.26	E	–	2.64
irx-9	14 17 45.94	+52 30 32.57	0.9853	1417	5.2	11.62	11.12	E	–	1.92
irx-10	14 18 21.86	+52 38 42.08	0.7197	1365	5.7	11.23		E	–	1.53
irx-11	14 19 38.59	+52 55 53.69	0.8976	1661	4.6	11.31	–	Sab	–	1.61
irx-12	14 20 38.87	+53 08 16.21	0.6873	1531	5.7	11.07	10.77	E	–	1.37
irx-13	14 21 16.46	+53 05 27.55	0.7433	1282	6.0	11.07	–	E	–	1.37
irx-14	14 22 38.98	+53 24 14.80	1.2873	2984	4.6	12.49	–	E	–	2.79
irx-15	12 36 29.13	+62 10 45.95	1.0130	1055	5.6	11.91	–	E	–	1.89
irx-16	12 36 56.01	+62 08 07.86	0.7920	1136	5.7	11.78	–	E	–	2.08
irx-17	12 36 46.61	+62 10 48.44	0.9399	912	5.1	11.41	–	Sab	0.35	1.39
irx-18	12 37 16.65	+62 17 33.56	1.1460	1112	4.5	11.48	11.23	Sab	0.2	1.78
irx-19	12 37 48.67	+62 13 12.84	0.9110	1641	5.5	–	11.75	QSO	1.50	–

The columns are (from left to right): Source identification; Right Ascension (J2000) of the IRAC 3.6 μm source; Declination (J2000) of the IRAC 3.6 μm source; spectroscopic redshift; observed $f_{24\,\mu m}/f_R$ flux ratio if the source were at $z = 2$; observed $R - [3.6]$ colour (AB system) if the source were at $z = 2$; log of the IR luminosity (3–1000 μm) of the starburst component, estimated from the SED spectral fits (a dash indicates that this component is not required to fit the data); log of the IR luminosity (3–1000 μm) of the AGN torus component, estimated from the SED spectral fits (a dash indicates that this component is not required to fit the data); best-fitting optical template in the optical; dust extinction; and log of the star formation rate estimated from the SED fits (a dash indicates no dust reddening).

IRX sources in the CDF-South ($S_{24} > 40$ μJy; Fiore et al. 2008) and 1 dex fainter than those in the COSMOS ($S_{24} > 500$ μJy; Fiore et al. 2009). We therefore conclude that our $z \approx 1$ sample, although not complete, is similar to the $z \approx 2$ IRX sources found in the CDF-South, for which Fiore et al. (2008) estimate a Compton thick rate of 80 ± 15 per cent and an intrinsic luminosity of $L_X(2–10\,\text{keV}) > 10^{43}$ erg s^{-1}.

4 SED FITTING

The observed optical to mid-IR SED of the sample sources are modelled following the methods fully described in Rowan-Robinson et al. (2005, 2008). In brief the *FUV*-band to 4.5 μm photometric data are fit using a library of eight templates described by Babbedge et al. (2004), six galaxies (E, Sab, Sbc, Scd, Sdm and sb) and two AGN. At longer wavelengths (5.8−24 μm) any dust may significantly contribute or even dominate the observed emission. Before fitting models to these wavelengths, the stellar contribution is subtracted from the photometric data by extrapolating the best-fitting galaxy template from the previous step. The residuals are then fit with a mixture of four templates: cirrus (Efstathiou & Rowan-Robinson 2003), AGN dust tori (Rowan-Robinson 1995; Efstathiou & Rowan-Robinson 1995), M 82 and Arp 220 starbursts (Efstathiou, Rowan-Robinson & Siebenmorgen 2000). The modelling above provides both information on the dominant emission mechanism in the optical and the infrared (AGN versus star formation) and an estimate of the total infrared luminosity, L_{TOT}, in the wavelength range 3–1000 μm. As discussed by Rowan-Robinson et al. (2005), L_{TOT} is expected to be accurate within a factor of 2. In this exercise the redshift is fixed to the spectroscopically determined value.

The results are presented in Table 1. Examples of template fits to SED of AEGIS and CDF-North sources are shown in Figs 4 and 5. Our analysis shows that dust associated with star formation (M82 starburst template) either dominates or substantially contributes to the flux at the mid-/far-infrared wavelengths of most sources. In this respect, it is not surprising that 12/14 galaxies in AEGIS and 4/5 sources in the CDF-N are detected at this longer wavelength. The estimated star formation rates are in the range 10–600 M$_\odot$ yr^{-1}. The best-fitting starburst template is that of M 82, in agreement with results from Bussmann et al. (2009b) who showed that the far-IR SEDs of IRX sources are better described by warm-dust templates (e.g. similar to M 82 or Mrk 231) and are inconsistent with cold dust templates (e.g. Arp 220).

An additional QSO torus component is required to fit the mid-IR part of the SED of some sources in Table 1. As will be shown in the next section, this component is needed only for those sources which are detected at X-ray wavelengths and which have intrinsic X-ray luminosities, $L_X(2–10\,\text{keV}) \gtrsim 10^{43}$ erg s^{-1}. The SED fitting approach can therefore be used to identify AGN with intrinsic luminosity $\gtrsim 10^{43}$ erg s^{-1}. Below this limit, star formation in the host galaxy may swamp any AGN signatures in the mid-IR.

5 X-RAY PROPERTIES

5.1 X-ray source counterparts

The cross-correlation between the X-ray and IRAC 3.6 μm catalogues using the likelihood ratio method shows that 5/16 and 4/5 of the sample sources in AEGIS and the CDF-North, respectively, have X-ray counterparts with Poisson significance $<4 \times 10^{-6}$ in at least one of the four energy bands used for detection. Lower significance X-ray counterparts are also searched for in the hard band (2–7 keV),

Table 2. Multiwavelength SEDs of the AEGIS IRX sources.

(1) ID	(2) u	(3) B	(4) g	(5) R	(6) r	(7) I	(8) i	(9) z	(10) 3.6 μm	(11) 4.5 μm	(12) 5.8 μm	(13) 8.0 μm	(14) 24 μm	(15) 70 μm
irx-1	-0.92 ± 0.12	-0.81 ± 0.10	-0.33 ± 0.04	0.45 ± 0.01	0.31 ± 0.01	0.93 ± 0.01	0.80 ± 0.01	0.97 ± 0.01	1.63 ± 0.01	1.43 ± 0.01	1.35 ± 0.01	1.29 ± 0.02	–	3.45 ± 0.05
irx-2	0.10 ± 0.03	0.04 ± 0.01	0.23 ± 0.01	0.43 ± 0.01	0.48 ± 0.01	0.76 ± 0.01	0.82 ± 0.01	0.95 ± 0.01	1.88 ± 0.01	2.06 ± 0.01	2.22 ± 0.01	2.68 ± 0.01	3.23 ± 0.01	3.70 ± 0.03
irx-3	-0.90 ± 0.12	-0.70 ± 0.10	-0.48 ± 0.04	0.27 ± 0.01	0.08 ± 0.02	0.74 ± 0.01	0.56 ± 0.01	0.71 ± 0.01	1.80 ± 0.01	1.64 ± 0.01	1.61 ± 0.01	1.66 ± 0.01	2.73 ± 0.01	3.50 ± 0.04
irx-4	-0.82 ± 0.22	-0.46 ± 0.10	-0.21 ± 0.03	0.41 ± 0.01	0.32 ± 0.01	0.98 ± 0.01	0.85 ± 0.01	1.09 ± 0.01	2.09 ± 0.01	1.95 ± 0.01	1.83 ± 0.01	1.92 ± 0.01	2.76 ± 0.01	3.33 ± 0.04
irx-5	-0.86 ± 0.14	-0.36 ± 0.04	0.03 ± 0.02	0.75 ± 0.01	0.64 ± 0.01	1.16 ± 0.01	1.09 ± 0.01	1.23 ± 0.01	1.90 ± 0.01	1.85 ± 0.01	1.89 ± 0.01	2.12 ± 0.01	2.76 ± 0.01	3.36 ± 0.04
irx-6	-0.83 ± 0.10	-0.83 ± 0.16	-0.41 ± 0.04	-0.04 ± 0.02	-0.01 ± 0.02	0.54 ± 0.01	0.40 ± 0.01	0.65 ± 0.01	1.72 ± 0.01	1.64 ± 0.01	1.44 ± 0.01	1.55 ± 0.01	2.45 ± 0.01	–
irx-7	-0.84 ± 0.10	-0.98 ± 0.20	-0.38 ± 0.03	0.15 ± 0.03	0.00 ± 0.02	0.65 ± 0.01	0.53 ± 0.01	0.74 ± 0.01	1.75 ± 0.04	1.61 ± 0.04	1.48 ± 0.04	1.53 ± 0.04	2.65 ± 0.01	–
irx-8	0.26 ± 0.02	0.11 ± 0.01	0.41 ± 0.01	0.93 ± 0.01	0.84 ± 0.01	1.39 ± 0.01	1.27 ± 0.01	1.49 ± 0.01	2.69 ± 0.01	2.89 ± 0.01	3.05 ± 0.01	3.30 ± 0.01	3.78 ± 0.01	4.14 ± 0.01
irx-9	-0.71 ± 0.14	-0.35 ± 0.04	-0.25 ± 0.03	0.38 ± 0.02	0.32 ± 0.01	0.98 ± 0.01	0.85 ± 0.01	1.13 ± 0.01	1.92 ± 0.01	1.92 ± 0.01	2.01 ± 0.01	2.33 ± 0.01	2.98 ± 0.01	3.59 ± 0.04
irx-10	-1.05 ± 0.16	-0.60 ± 0.08	-0.44 ± 0.04	0.23 ± 0.02	0.02 ± 0.02	0.59 ± 0.01	0.45 ± 0.01	0.63 ± 0.01	1.68 ± 0.01	1.51 ± 0.01	1.55 ± 0.01	1.55 ± 0.01	2.60 ± 0.01	3.53 ± 0.04
irx-11	-0.86 ± 0.13	-0.70 ± 0.11	-0.33 ± 0.03	0.12 ± 0.01	0.07 ± 0.02	0.56 ± 0.01	0.45 ± 0.01	0.63 ± 0.01	1.31 ± 0.04	1.10 ± 0.04	0.94 ± 0.04	1.01 ± 0.04	–	3.38 ± 0.05
irx-12	-0.58 ± 0.06	-0.46 ± 0.08	-0.06 ± 0.02	0.62 ± 0.01	0.49 ± 0.01	1.07 ± 0.01	0.92 ± 0.01	1.09 ± 0.01	2.03 ± 0.01	2.03 ± 0.01	2.09 ± 0.01	2.35 ± 0.01	2.88 ± 0.01	3.67 ± 0.02
irx-13	-1.39 ± 0.45	-0.58 ± 0.16	-0.55 ± 0.04	0.38 ± 0.01	0.06 ± 0.02	0.86 ± 0.01	0.57 ± 0.01	0.76 ± 0.01	1.71 ± 0.01	1.54 ± 0.01	1.51 ± 0.01	1.51 ± 0.01	2.46 ± 0.01	3.34 ± 0.05
irx-14	–	-0.43 ± 0.06	–	0.08 ± 0.02	–	0.51 ± 0.04	–	–	1.75 ± 0.04	1.80 ± 0.04	1.65 ± 0.04	1.89 ± 0.04	–	4.00 ± 0.01

None of the sources is detected in the GALEX FUV band. Source irx-8 has a GALEX NUV log flux density of 0.10 ± 0.03 (μJy units). The columns are: (1): Source identification: (2) log of CFHTLS u-band flux density in units of μJy; (3) log of DEEP2B-band flux density in units of μJy; (4) log of DEEP2R-band flux density in units of μJy; (5) log of DEEP2R-band flux density in units of μJy; (6) log of CFHTLS r-band flux density in units of μJy; (7) log of DEEP2I-band flux density in units of μJy; (8) log of CFHTLS i-band flux density in units of μJy; (9) log of CFHTLS z-band flux density in units of μJy; (10) log of IRAC 3.6 μm band flux density in units of μJy; (11) log of IRAC 4.5 μm band flux density in units of μJy; (12) log of IRAC 5.8 μm band flux density in units of μJy; (13) log of IRAC 8.9 μm band flux density in units of μJy; (14) log of MIPS 24 μm band flux density in units of μJy; (15) log of MIPS 70 μm band flux density in units of μJy.

Table 3. Multiwavelength SEDs of the CDF-North IRX sources.

(1) ID	(2) U	(3) B	(4) R	(5) I	(6) z	(7) 3.6 μm	(8) 4.5 μm	(9) 5.8 μm	(10) 8.0 μm	(11) 24 μm	(12) 70 μm
irx-15	-0.69 ± 0.05	-0.52 ± 0.04	0.11 ± 0.01	0.59 ± 0.01	0.78 ± 0.01	1.91 ± 0.01	1.87 ± 0.01	1.84 ± 0.01	1.80 ± 0.02	2.73 ± 0.01	3.24 ± 0.07
irx-16	-0.70 ± 0.04	-0.30 ± 0.03	0.57 ± 0.01	1.00 ± 0.01	1.17 ± 0.01	2.00 ± 0.01	1.85 ± 0.01	1.88 ± 0.01	1.89 ± 0.02	2.85 ± 0.01	4.09 ± 0.02
irx-17	-0.83 ± 0.05	-0.75 ± 0.05	-0.04 ± 0.01	0.39 ± 0.01	0.54 ± 0.01	1.49 ± 0.01	1.37 ± 0.01	1.39 ± 0.04	1.34 ± 0.04	2.47 ± 0.01	3.39 ± 0.05
irx-18	-0.44 ± 0.02	-0.33 ± 0.04	0.22 ± 0.01	0.57 ± 0.01	0.71 ± 0.01	1.73 ± 0.01	1.86 ± 0.01	2.07 ± 0.01	2.31 ± 0.01	2.99 ± 0.01	3.41 ± 0.06
irx-19	-0.94 ± 0.08	-0.80 ± 0.05	0.13 ± 0.01	0.64 ± 0.01	0.83 ± 0.01	1.56 ± 0.01	1.65 ± 0.01	1.91 ± 0.01	2.12 ± 0.01	2.53 ± 0.01	–

None of the sources is detected in the GALEX NUV and FUV bands. The columns are: (1) Source identification; (2) log of U-band flux density in units of μJy; (3) log of B-band flux density in units of μJy; (4) log of DEEP2R-band flux density in units of μJy; (5) log of DEEP2I-band flux density in units of μJy; (6) log of CFHTLS z-band flux density in units of μJy; (7) log of IRAC 3.6 μm-band flux density in units of μJy; (8) log of IRAC 4.5 μm-band flux density in units of μJy; (9) log of IRAC 5.8 μm-band flux density in units of μJy; (10) log of IRAC 8.9 μm-band flux density in units of μJy; (11) log of MIPS 24 μm-band flux density in units of μJy; (12) log of MIPS 70 μm-band flux density in units of μJy.
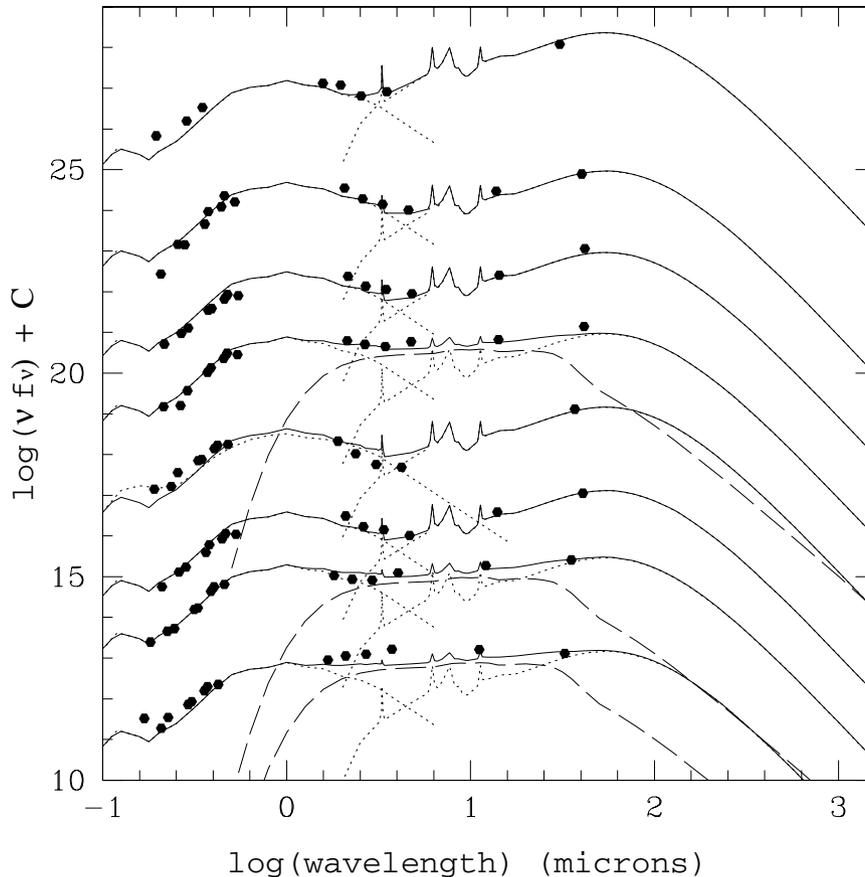
Figure 4. Examples of template fits to the SEDs of the IRX selected galaxies in the AEGIS. From bottom to top are: irx-8 (X-ray source), irx-9 (X-ray source), irx-10, irx-11, irx-12 (X-ray source), irx-13, irx-14 and irx-7. The dots are the observed UV–to–far-IR photometry and the continuous lines are the best-fitting models. Different sources are offset by an arbitrary constant for clarity. The dashed curves correspond to the hot dust torus component, which is needed for all X-ray detected sources with $L_X(2\text{–}10\,\text{keV}) \gtrsim 10^{43}\,\text{erg s}^{-1}$. The dotted lines at infrared wavelengths are the starburst components.

which provides a reasonable compromise between sensitivity and obscuration effects, thereby minimizing biases when extrapolating fluxes to the rest-frame energy range of 2–10 keV. The X-ray counts within the 70 per cent encircled energy fraction (EEF) radius at the position of each source in Table 1 are summed up and a local value for the background is estimated using an annulus centred on the source with inner radius 1.5 times the 90 per cent EEF and width of 50 arcsec (100 pixels). For the estimation of the background, X-ray sources with Poisson significance $<4 \times 10^{-6}$ are removed by excluding pixels within the 95 per cent EEF radius of each source. The probability that the observed counts are a random fluctuation of the background is estimated using Poisson statistics. We consider as detections sources with Poisson significance $<3 \times 10^{-3}$. This exercise yields two lower-significance X-ray detections, one in the AEGIS and one in the CDF-N. The fluxes of these sources are estimated using a Bayesian methodology similar to that described in Laird et al. (2009). For a source with observed number of total counts N (source and background) within the 70 per cent EEF radius and a local background value B, the probability of flux f_X is

$$P(f_X, N) = \frac{T^N e^{-T}}{N!}\,\pi(f_X),\tag{1}$$

where $N = S + B$ and $S = f_X \times t_{\text{exp}} \times C \times \eta$. In the last equation, t_{exp} is the exposure time at a particular position after accounting for instrumental effects, C is the conversion factor from flux to count rate and η is the EEF, i.e. 0.7 in our case. The term $\pi(f_X)$ in equation (1) accounts for the Eddington bias and assumes that the differential

X-ray source counts follow a broken power law for the log N − log S with faint and bright-end slopes of −1.5 and −2.5, respectively, and a break flux of $10^{-14}\,\text{erg s}^{-1}\,\text{cm}^{-2}$ (Georgakakis et al. 2008). For the source flux, we adopt the mode of the distribution $P(f_X, N)$.

The same methodology is also adopted to estimate upper limits for the fluxes of the sources that are not detected at X-ray wavelengths. The confidence interval CL is given by the integral

$$\int_{f_{X,L}}^{f_{X,U}} P(f_X, N)\,df_x = CL.\tag{2}$$

For a faint-end slope of −1.5, the integral diverges at the faintest fluxes. To avoid this problem we adopt as the lower limit of the integration $f_{X,L} = 10^{-18}\,\text{erg s}^{-1}\,\text{cm}^{-2}$. Equation (2) is then solved numerically to estimate the flux upper limit $f_{X,U}$ for the confidence interval of 99.97 per cent. The results are presented in Table 1.

5.2 X-ray spectral analysis

The X-ray spectra of the sample sources were extracted using the ACIS extract (AE; v. 2008-03-04; Broos et al. 2002) IDL package, which is designed to deal with large number of sources on multiple observations. The AE package User's Guide is available online at http://www.astro.psu.edu/xray/docs/TARA/ae_users_guide. html. The procedures used in AE are described in Townsley et al. (2003) and Getman et al. (2005). The X-ray counts of each source were extracted from individual pointings using the 95 per cent
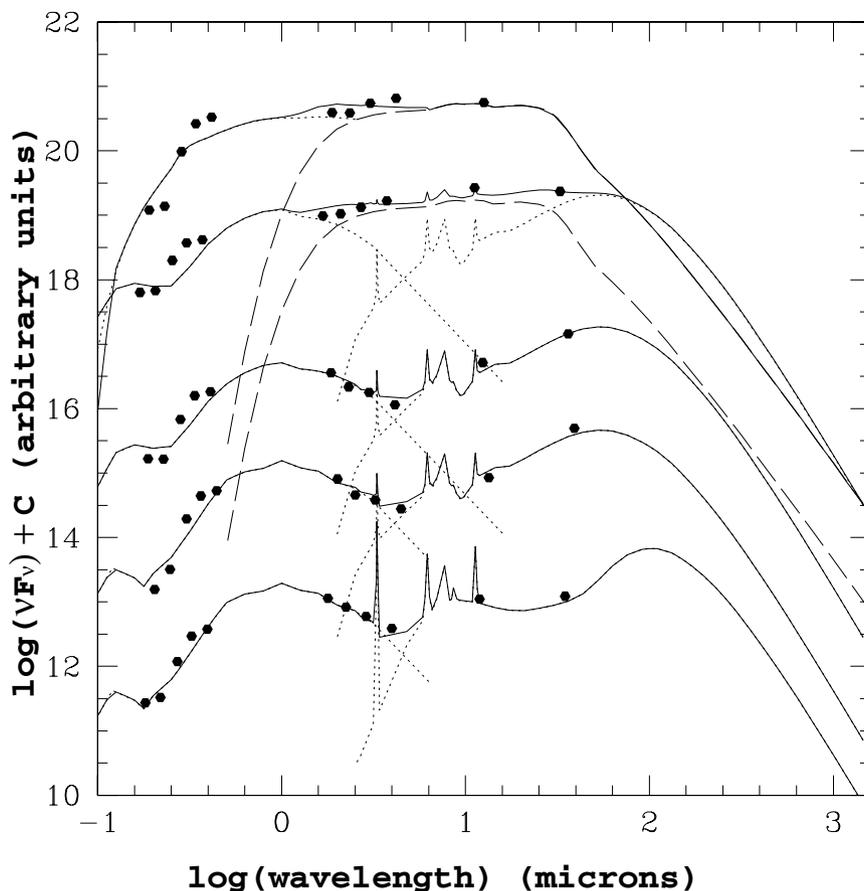
Figure 5. Same as in Fig. 4 for IRX selected galaxies in the CDF-North. From bottom to top are: irx-15, irx-16, irx-17, irx-18, irx-19. The curves and dots are the same as in Fig. 4.

encircled energy radius (1.5 keV) at the position of the source. The composite source spectrum was then constructed by summing the counts from each observation. For the background estimation, point sources were first masked out using a circular region with size 1.1 larger than the 99 per cent EEF at 1.5 keV. The background spectra were then extracted from the masked event files of individual observations using an annulus centred on the source with variable size that enclosed at least 150 background counts. The spectra from separate pointings were scaled by the ratio of the exposure time in the source and background regions and then summed up into the composite background spectrum for a particular source. The response matrix files (RMF) and area response files (ARF) for individual observations were constructed using the CIAO tools MKACISRMF and MKARF, respectively. These were then combined into composite RMFs and ARFs by the FTOOL tasks ADDRMF and ADDARF, respectively, using the exposure time of each observation as weight. Source spectra were grouped to have at least one count per bin.

For the spectral fits we use the XSPEC v12. We adopt a realistic AGN spectral model to fit the data, motivated by current observations and ideas about the structure of the regions close to SBHs. The model consists of power law absorbed by cold material and a reflection component as described below.

The main spectral component of AGN is the power law with an average photon index $\Gamma = 1.9$ (Nandra & Pounds 1994) and a cut-off at high energies (≈ 100 keV; Gondek et al. 1996). The dispersion around the mean Γ is estimated to be 0.2–0.3 (Gondek et al.

1996). The reflection component represents direct AGN emission that intersects optically thick material, such as the accretion disk or the torus, and is Compton backscattered into the line of sight. We parametrize this component using the PEXMON model of XSPEC (Nandra et al. 2007), which includes an analytic formulation for the strength of the narrow iron line at 6.4 keV, which is expected to be prominent in the reflection spectrum. The direct emission of AGN is also modified by cold material. We adopt the photoelectric absorption cross-sections of Morrison & McCammon (1983) for solar metallicity to represent any cold absorbing medium, such as a torus. Ideally, our modelling should also include absorption by ionized material. However, given the relatively small number of counts in the typical X-ray spectra of deep field sources, we choose not to include this component in the analysis. In any case, warm absorption is predominantly affecting the AGN spectra at soft energies $\lesssim 1$ keV (e.g. George et al. 1998). At least part of the warm absorber spectral features are therefore expected to be redshifted out of the *Chandra* observable energy range for sources at moderate and high redshifts. We also perform the spectral modelling for source photons >2 keV (observer's frame) to ensure that soft emission associated with a warm absorber does not modify the results and conclusions. In summary, the XSPEC model we are using consists of a power law absorbed by cold gas at the rest frame of the source and Compton reflection. These components are also absorbed by cold gas in our Galaxy using the appropriate Galactic H I column density for the AEGIS ($N_H = 1.4 \times 10^{20}$ cm^{-2}) and the CDF-North ($N_H = 1.3 \times 10^{20}$ cm^{-2}). In XSPEC terminology, our

Table 4. X-ray properties of the sample.

(1) ID	(2) XID	(3) Counts	(4) bkg	(5) N_H ($\times 10^{22}$ cm^{-2})	(6) R	(7) Γ	(8) c-stat	(9) d.o.f.	(10) L_X(2–10 keV) ($\times 10^{43}$ erg s^{-1})
irx-1	–	16	7.3	–	–	–	–	–	<0.7
irx-2	egs_0263	127	0.6	$44.6^{+26.0}_{-12.1}$	$0.6^{+1.2}_{-0.6}$	1.9(f)	42.1	46	36.4
irx-3	–	0	0.2	–	–	–	–	–	<0.07
irx-4 i	–	4	0.5	–	–	–	–	–	0.1
irx-5	egs_0311	112	5.9	$7.9^{+2.9}_{-2.5}$	$2.3^{+8.0}_{-2.9}$	1.9(f)	40.5	46	3.2
irx-6	–	14	10.4	–	–	–	–	–	<0.6
irx-7	–	2	0.2	–	–	–	–	–	<0.9
irx-8	egs_0416	820	1.0	$2.1^{+0.6}_{-0.8}$	$0.03^{+7.8}_{-0.03}$	$2.1^{+0.7}_{-0.2}$	48.2	45	27.9
irx-9	egs_0424	254	1.2	$4.6^{+1.1}_{-1.1}$	$0.5^{+2.7}_{-0.5}$	1.9(f)	44.9	46	8.8
irx-10	–	0	0.1	–	–	–	–	–	<0.1
irx-11	–	6	4.1	–	–	–	–	–	<0.4
irx-12	egs_0917	163	47.0	$10.3^{+3.5}_{-3.5}$	$2.6^{+10.7}_{-2.6}$	1.9(f)	43.4	46	2.4
irx-13	–	19	11.8	–	–	–	–	–	<0.4
irx-14	–	2	0.2	–	–	–	–	–	<1.2
irx-15	hdfn_098	174	28.0	$9.5^{+5.7}_{-4.6}$	$6.4^{+22.8}_{-6.4}$	1.9(f)	41.4	39	0.6
irx-16	hdfn_328	129	96.7	$1.3^{+4.1}_{-1.3}$	-1(f)	1.9(f)	50.3	47	0.05
irx-17	hdfn_466	27	20.5	<2.8	-1(f)	1.9(f)	43.1	49	0.046
irx-18	hdfn_023	2240	74.2	$2.3^{+0.8}_{-0.6}$	$5.6^{+22.5}_{-2.5}$	$2.0^{+0.7}_{-0.3}$	51.4	45	9.3
irx-19	–	260	210.1	$55.4^{+117.5}_{-38.2}$	$0.2^{+18.4}_{-0.2}$	1.9(f)	103.5	117	0.7

The columns are: (1) Source identification; (2) X-ray identification number as in Laird et al (2009) for AEGIS and Georgakakis et al. (2008) for the CDF-North. Sources without an X-ray counterpart or low significance (Poisson probability $>4 \times 10^{-6}$) X-ray sources do not have an X-ray identification number (3) total counts in the energy range 0.5–10 keV. For sources with insufficient counts to perform X-ray spectral analysis the total extracted counts in the 2–8 keV band are listed. (4) background counts in the range 0.5–10 keV. For sources with insufficient counts to perform X-ray spectral analysis the background counts in the 2–8 keV band are listed. (5) best-fitting column density of the cold absorber (WABS component of XSPEC model). The uncertainties correspond to the 90 per cent confidence level; (6) reflection fraction of the PEXMON model of XSPEC. The errors correspond to the 90 per cent confidence level; (7) power-law photon index, Γ, of the intrinsic AGN power-law spectrum. The '(f)' indicates that this parameter was kept fixed in the fit. (10) C-stat of the best-fitting solution; (9) degrees of freedom; (11) obscuration corrected luminosity in the 2–10 keV range and in units of 10^{43} erg s^{-1}. In the case of upper limits or sources with insufficient counts to perform X-ray spectral analysis, no correction has been applied for intrinsic obscuration. In those sources fluxes and luminosities in the 2–10 keV band are estimated by adopting a power-law spectral index with $\Gamma = 1.4$, i.e. assume that the sources have X-ray spectra similar to that of the X-ray background. The statistical uncertainty in the luminosity is less than 10 per cent for X-ray detected sources (Poisson probability $<4 \times 10^{-6}$) and about a factor of 2 for low-significance ones.

model is wabs × (zwabs × po + pexmon), where wabs and zwabs are the cold absorption from our Galaxy and at the rest frame of the sources, respectively, and po is the power law.

The parameters of the model are the photon index and the high-energy cut-off (pexmon only) of the direct AGN emission; the column density of the cold absorber, N_H; the element abundances; the inclination i of the slab that gives the reflection and the reflection fraction R, defined as the strength of the reflection relative to that expected from a slab subtending a solid angle of 2π;. Clearly, there are too many free parameters given the number of counts in our spectra (see Table 4). We therefore fix abundances to solar values and the inclination angle to 60 deg. Given that the spectra cover the energy range of 2–10 keV (rest frame 4–20 keV at $z \approx 1$), the energy cut-off of the direct AGN emission will have negligible impact on the results. We therefore choose to fix this parameter to 1000 keV (pexmon only). These assumptions leave three free parameters: Γ, N_H and R. For X-ray sources in the sample with <200 net counts in the 0.5–10 keV range, we also fix the photon index of the power law to $\Gamma = 1.9$, while for sources with <50 net counts we further fix the reflection fraction to $R = 1$.

In the case of Compton thick AGN, we expect either to see directly the turnover in the spectrum at rest-frame energies $\gtrsim 15$ keV because of the cold absorption (i.e. estimate a column density $N_H > 2 \times 10^{24}$ cm^{-2} from the spectral fit) or get a reflection-dominated spectrum with $R \gg 10$ (Nandra et al. 2007).

Spectral analysis was performed for sources with sufficient number of net counts to place meaningful constraints. This requirement excluded from the spectral fits sources with low-significance X-ray counterparts, except one – irx-19. This source lies just below the formal detection threshold of the CDF-North source catalogue. The results of the spectral analysis are summarized in Table 4. Spectral fits for individual sources are shown in Figs 6 and 7. All sources in the sample are consistent with moderate column densities in the range $N_H \approx 10^{22} - 5 \times 10^{23}$ cm^{-2}, while the best-fitting relative reflection parameter is <10 for all of them. For four sources, however, the 90 per cent upper limit in R is greater than 10. For one of them, irx-19, the 90 per cent upper limit for the column density is $N_H = 1.2 \times 10^{24}$ cm^{-2}, close to the Compton thick limit ($N_H = 2 \times 10^{24}$ cm^{-2}). Another of the four sources, irx-18, also shows the Fe Kα 6.4 keV in the X-ray spectrum with a rest-frame equivalent width of $EW = 0.5 \pm 0.2$ keV. Although a strong Fe Kα line (EW $\gtrsim 1$ keV; Ghisellini, Haardt & Matt 1994) is evidence for Compton thick AGN, the estimated EW is also consistent with Compton thin obscuration. We conclude that the X-ray spectral analysis suggests that two sources in the sample show tentative evidence for Compton thick obscuration.

Also, the X-ray emission of two X-ray detected sources (irx-16 and irx-17) is likely associated with starburst activity, not accretion on a central supermassive black hole. These two sources have L_X(2–10 keV) $\approx 5 \times 10^{41}$ erg s^{-1}, relatively soft, albeit noisy, X-ray
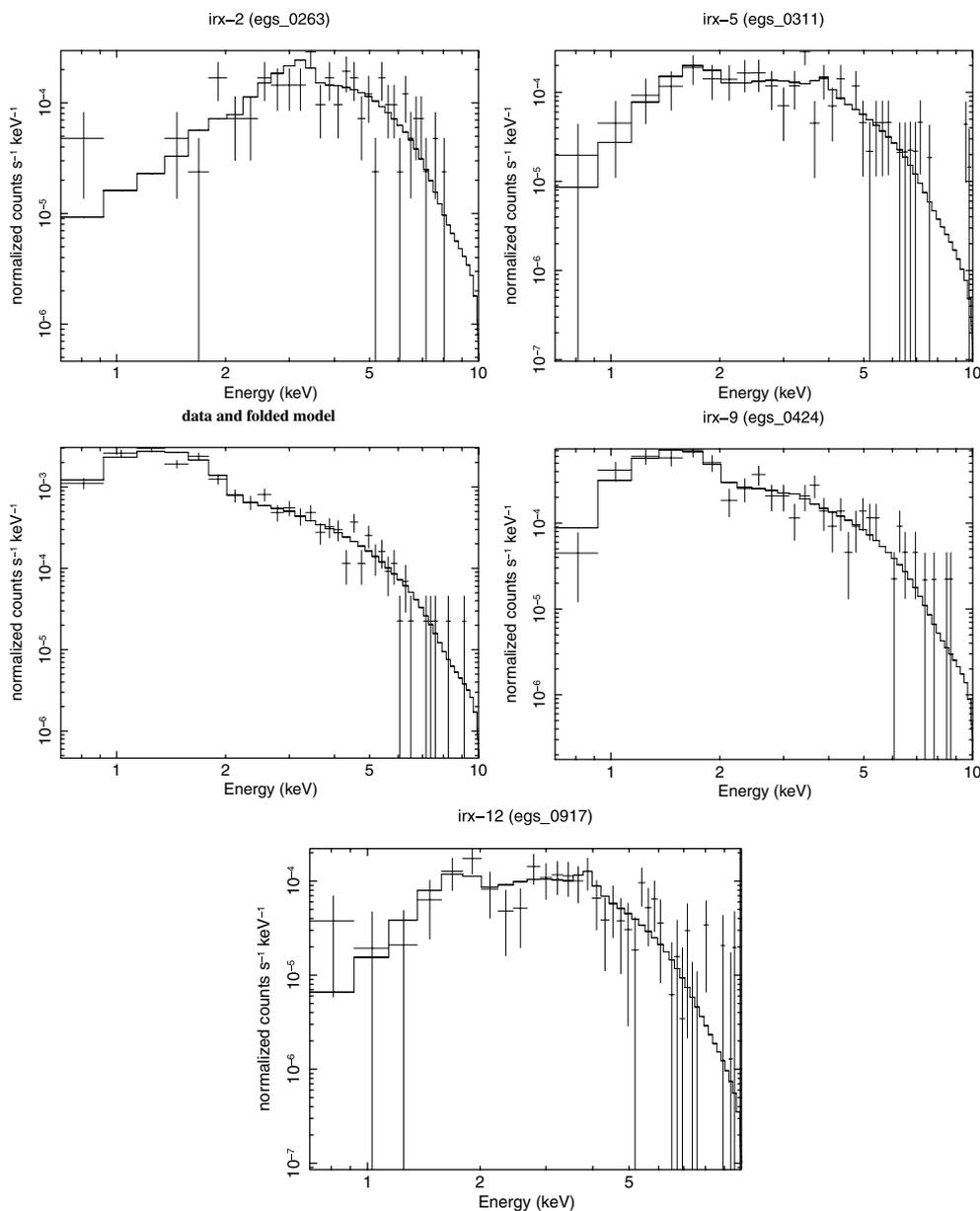
Figure 6. X-ray spectra and spectral fits for the IRX sources in the AEGIS.

spectra and follow the correlation between X-ray and infrared luminosities for star-forming galaxies (Ranalli, Comastri & Setti 2003) as shown in Fig. 8. Their infrared SEDs are also consistent with starburst templates and do not require an additional hot dust component associated with the AGN torus. Fig. 8 also demonstrates that a QSO torus component is required to fit the mid-IR part of the SED of only those sources in Table 1 which are detected at X-ray wavelengths and which have X-ray luminosity, $L_X(2\text{--}10\,\text{keV}) \gtrsim 10^{43}\,\text{erg s}^{-1}$. The SED fitting method of Section 4 is therefore sensitive to AGN with intrinsic X-ray luminosity above this limit.

6 DISCUSSION AND CONCLUSIONS

The population of IRX galaxies has attracted much attention recently as they are proposed as good candidates for Compton thick QSOs at $z \approx 2$ with luminosities $L_X(2\text{--}10\,\text{keV}) > 10^{43}\,\text{erg s}^{-1}$. The low X-ray-to-mid-IR luminosity ratio and the mean hardness ratios

of these sources are consistent with this interpretation as long as the bulk of the mid-IR luminosity is associated with the dust heated by the central engine. There are indications, however, that this is not the case, at least not for all IRX sources. Murphy et al. (2009) combined mid-IR spectroscopy with far-IR submillimetre data to show that only 50 per cent of the infrared excess sources selected in a way similar to that described by Daddi et al. (2007), show evidence for obscured AGN activity. The other half of this population have SEDs consistent with star formation. Yan et al. (2007) presented *Spitzer*–IRS spectra of 52 galaxies brighter than 1 mJy at 24 μm selected in the *Spitzer* extragalactic First Look Survey (xFLS). The relative strengths of the AGN and starburst components in those sources have been estimated by Sajina et al. (2008) using, in addition to the mid-IR spectroscopy, multiwavelength photometric observations (UV to far-IR and radio), optical and NIR spectroscopy. There are 21 sources in the Yan et al. (2007) sample with properties similar to the IRX population at $z \approx 2$, i.e. $f_{24\,\mu\text{m}}/f_R > 900$ and
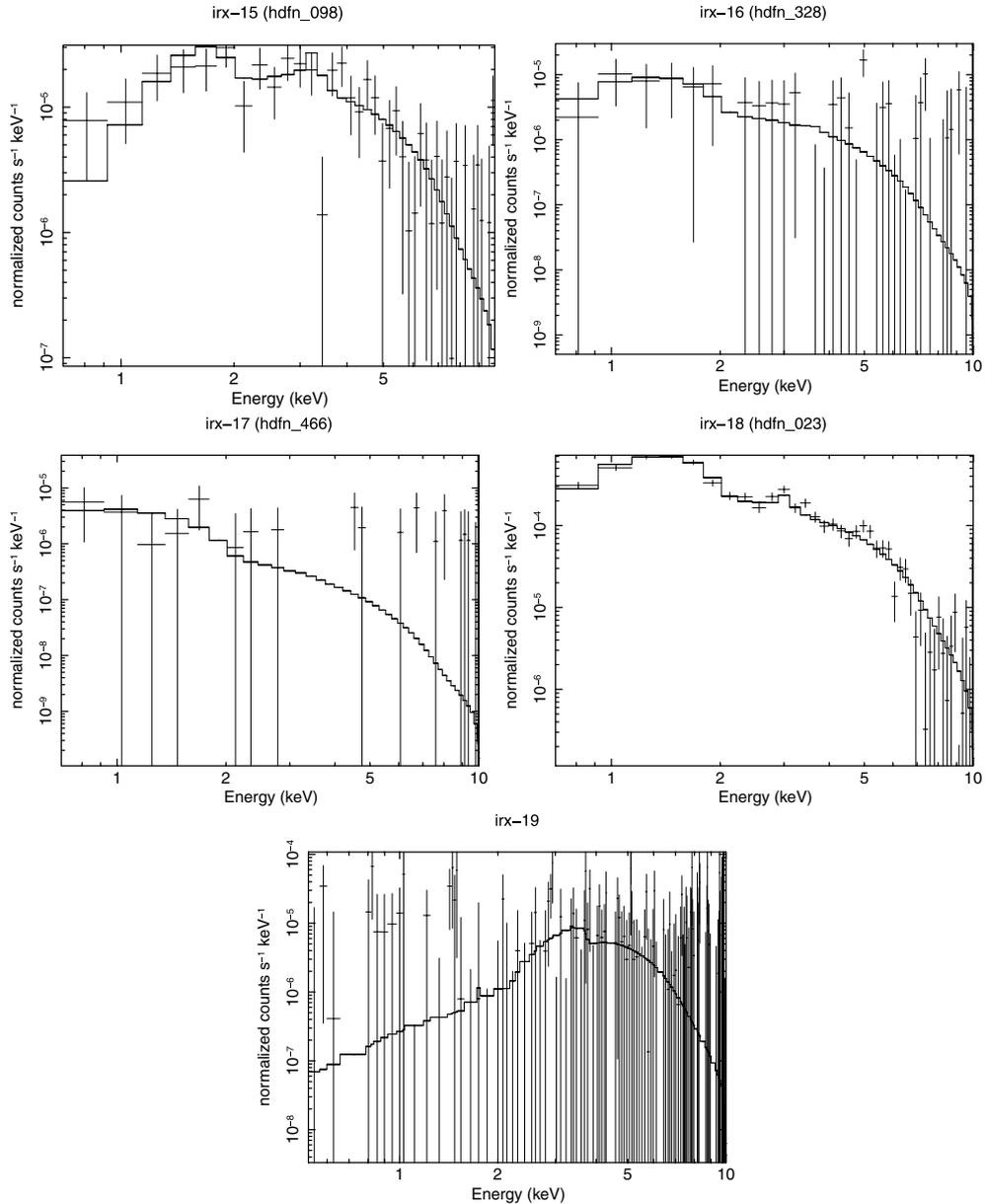
Figure 7. X-ray spectra and spectral fits for the IRX sources in the CDF-North.

spectroscopic redshift determination $z > 1.5$. Sajina et al. (2008) found that about 76 per cent (16/25) of those sources are AGN dominated in the IR, while the remaining 24 per cent have starburst components that either dominate or contribute nearly equally to the AGN at IR wavelengths. If star formation contributes to the mid-IR luminosity of IRX galaxies then the two key properties of this population, X-ray–to–mid-IR luminosity ratio and mean hardness ratio, are also consistent with either lower-luminosity Compton thin AGN (e.g. Figs 1 and 2) or pure starbursts (Donley et al. 2008).

In order to shed more light in the nature of IRX sources, we select galaxies at $z \approx 1$ in the AEGIS and CDF-North fields with SEDs similar to the $z \approx 2$ IRX population. The advantage of this approach is that the selected sources have fluxes that are brighter at almost any wavelength compared to IRX galaxies at $z \approx 2$, thereby greatly facilitating their study.

It is interesting that about 35 per cent of the sources in the AEGIS (5/14) and 80 per cent in the CDF-North (4/5) are associated with

hard (2–7 keV) X-ray detections with significance $<4 \times 10^{-6}$. These fractions increase to 43 (6/14) and 100 (5/5) per cent in the AEGIS and CDF-N, respectively, if lower significance sources are included. For comparison, only about 4 per cent of red cloud galaxies in the AEGIS have X-ray counterparts (Nandra et al. 2007). This suggests a high AGN identification rate in samples selected using the infrared excess criteria.

Excluding X-ray detected starburst candidates (irx-16 and irx-17), the IRX sources with X-ray counterparts are indeed AGN, as indicated by their X-ray luminosities, $L_X(2–10\,\text{keV}) > 10^{42}\,\text{erg s}^{-1}\,\text{cm}^{-2}$, which are higher than what can be attributed to star formation (Georgakakis et al. 2007). These sources also have hard X-ray spectral properties, which are however consistent with Compton thin column densities, $N_{\text{H}} \approx 10^{22} - 5 \times 10^{23}\,\text{cm}^{-2}$. There is only tentative evidence for Compton thick obscuration among the X-ray-detected IRX sources. For four of them, the 90 per cent upper limit of the reflection fraction is higher than $R = 10$. Also,
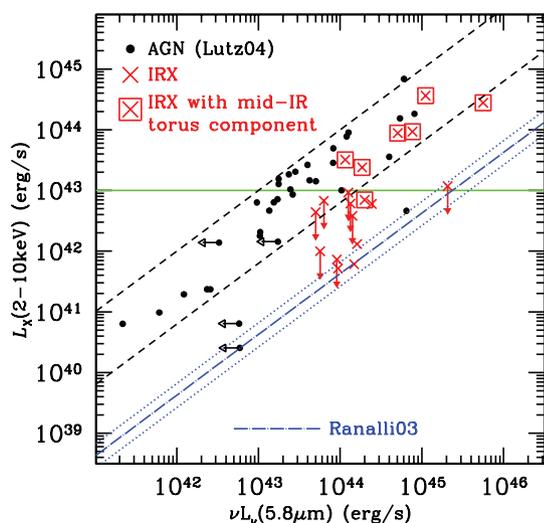
Figure 8. X-ray 2–10 keV luminosity plotted against 5.8 μm luminosity. Filled circles (black) are local AGN from the sample of Lutz et al. (2004). The dashed lines show the dispersion around the mean $L_X(2\text{–}10\,\text{keV}) - \nu L_\nu(5\,\mu\text{m})$ relation for the Lutz et al. (2004) AGN. The (blue) long-dashed–dotted line is the $L_X - \nu L_{5\,\mu\text{m}}$ relation for star-forming galaxies adapted from (Ranalli et al. 2003; see Fiore et al. 2009). The dotted lines correspond to the 1 sigma rms envelope around this relation. Our sample of IRX sources is shown with the (red) crosses. For IRX sources that are not detected at X-ray wavelengths the upper limit in $L_X(2\text{–}10\,\text{keV})$ is plotted. A square on top of a cross signifies IRX sources which require a torus component to fit their infrared SEDs. Above an intrinsic X-ray luminosity of $10^{43}\,\text{erg s}^{-1}$ (shown with the horizontal green line) all IRX sources with an X-ray counterpart in the 2–10 keV band require a torus component.

the X-ray spectra of two of those four sources either have 90 per cent upper limit in the column density $\approx 1.2 \times 10^{24}\,\text{cm}^{-2}$ or show the Fe Kα 6.4-keV line with an equivalent width of 0.5 keV. These properties can be interpreted as evidence for Compton thick AGN but are also consistent with Compton thin obscuration.

More relevant to the deeply buried AGN picture are the infrared excess sources in the sample that are not detected at X-ray wavelengths. The SED modelling shows that their mid- and far-IR are dominated by star formation and that there is no indication for a hot dust component associated with a powerful AGN that remains undetected at X-ray wavelengths. It is noted that the QSO torus template is required to fit the IR SEDs of *all* X-ray-detected AGNs with intrinsic X-ray luminosities brighter than $L_X(2\text{–}10\,\text{keV}) \approx 10^{43}\,\text{erg s}^{-1}$. Therefore, if some of the X-ray-undetected sources were associated with heavily obscured and powerful AGNs with X-ray emission suppressed by the intervening dust and gas clouds, we would have identified them in the mid-IR as sources with a QSO torus component. We can therefore place an upper limit of $L_X(2\text{–}10\,\text{keV}) = 10^{43}\,\text{erg s}^{-1}$ to the intrinsic AGN luminosity of X-ray-undetected sources, if they host an active SBH. We conclude that the IRX sources without X-ray counterparts in our sample are either starbursts, lower-luminosity AGNs or a combination of the two.

This result has implications on the nature of the $z \approx 2$ IRX population detected in deep surveys. There is no doubt that some of these sources are Compton thick QSOs. Georgantopoulos et al. (2009), for example, identified Compton thick QSOs among X-ray sources in the CDF-North through X-ray spectroscopy and showed that some of them satisfy the infrared excess selection criteria. Our analysis, however, shows that a potentially

large fraction of the IRX population at $z \approx 2$ are not luminous $[L_X(2\text{–}10\,\text{keV}) > 10^{43}\,\text{erg s}^{-1}]$ Compton thick QSOs but lower-luminosity $[L_X(2\text{–}10\,\text{keV}) < 10^{43}\,\text{erg s}^{-1}]$, possibly Compton thin, AGNs and/or starbursts.

Dust-enshrouded star formation has already been proposed as an alternative to Compton thick QSOs to explain the properties of the $z \approx 2$ IRX sources. Donley et al. (2008) critically reviewed different methods proposed in the literature for finding AGNs at infrared wavelengths, including the infrared excess selection. They showed that the red SED of these sources are consistent with those of local pure starbursts with some moderate amounts of additional reddening at optical wavelengths ($A_V \sim 1$ mag). They also cautioned that the stacked X-ray signal of this population may be dominated by a few sources. Moreover, they argued that flat mean X-ray spectral properties of the IRX population could be the result of high-mass X-ray binaries, which are known to have hard X-ray spectral properties (power laws with $\Gamma \approx 1.2$). Whether binary stars can dominate the integrated X-ray emission of local starbursts is, however, still under debate. In any case, based on the arguments above, Donley et al. (2008) suggested that as much as half of the IRX population at $z \approx 2$ are starbursts with only about 20 per cent showing evidence for heavily obscured, possibly Compton thick, AGN activity. Pope et al. (2008) analysed the mid-IR spectra of 12 IRX sources with $f_{24\,\mu\text{m}} > 300\,\mu\text{Jy}$ in the GOODS-North and found that six of them are dominated by star formation at the mid-IR. They also showed that AGN and starburst-dominated IRX sources have distinct 8.0 μm over 4.5 μm flux ratios, $f_{8.0\,\mu\text{m}}/f_{4.5\,\mu\text{m}}$. Extrapolating their results to fainter IRX sources $f_{24\,\mu\text{m}} = 100\text{–}300\,\mu\text{Jy}$, for which mid-IR spectroscopy is not available, they found that about 80 per cent of them have $f_{8.0\,\mu\text{m}}/f_{4.5\,\mu\text{m}}$ consistent with star formation. They also estimate the mean SED of IRX sources in their sample and conclude that less than about 10 per cent of the total infrared luminosity (8–1000 μm) is associated with hot dust, possibly heated by an AGN. For the average infrared luminosity of the Pope et al. (2008) sample, $L_{\text{IR}} = 10^{12}\,\text{L}_\odot$, the fraction above translates to an upper limit in the AGN luminosity of $L_{\text{IR}} \approx 4 \times 10^{44}\,\text{erg s}^{-1}$. Adopting the AGN bolometric correction factors $L_{\text{bol}}/L_{\text{IR}} = 3$ (Risaliti & Elvis 2004) and $L_{\text{bol}}/L_X(2\text{–}10\,\text{keV}) = 35$ (Elvis et al. 1994), we estimate a mean hard X-ray luminosity $L_X(2\text{–}10\,\text{keV}) < 3 \times 10^{43}\,\text{erg s}^{-1}$. Although there are uncertainties in this calculation, there is broad agreement in the upper limits in L_X estimated for the Pope et al. (2008) and our sample of IRX sources.

The sample presented here has properties similar to moderately bright IRX sources at $z \approx 2$, i.e. 5.8 μm luminosity a few times $10^{44}\,\text{erg s}^{-1}$, like those found in the CDF-South by Fiore et al. (2008). The simulations of Narayanan et al. (2009) suggest that IRX sources above $S_{24} = 300\,\mu\text{Jy}$ are dominated by gaseous mergers and include a large fraction of powerful AGN, whereas less luminous systems, like those studied here, are typically secularly evolving galaxies dominated by star formation and with only weak AGN activity. Our results on the nature of moderately luminous IRX sources are therefore consistent with those simulation. It is likely that IRX sources more luminous than those studied here (i.e. COSMOS field, $S_{24} > 500\,\mu\text{Jy}$, $\nu L_\nu(5.8\,\mu\text{m}) > 10^{45}\,\text{erg s}^{-1}$; Fiore et al. 2009) include a higher fraction of Compton thick QSOs. The results of Sajina et al. (2008) on the nature of bright ($S_{24} > 900\,\mu\text{Jy}$) IRX sources selected in the xFLS (Yan et al. 2007) suggest that this may be the case. Bauer et al. (2010) explored the X-ray properties of a subset of the Yan et al. (2007) sample and found evidence for at least mildly Compton thick ($N_{\text{H}} \approx 10^{24}\,\text{cm}^{-2}$) obscuration in a large fraction of the sources that are AGN dominated in the mid-IR. Even at the extreme luminosities of the xFLS sample, however, a

non-negligible fraction of the IRX sources (about 24 per cent) have a substantial or even dominant starburst component in the mid-IR. This underlines the importance for subtracting the contribution of star formation to the mid-IR to assess the intrinsic AGN luminosity before concluding whether the X-ray/mid-IR properties of these systems are consistent with Compton thick obscuration.

Mullaney et al. (2009) have recently found that the X-ray to total infrared luminosity ratios of X-ray AGN with $L_X(2-10\,\text{keV}) = 10^{42}-10^{43}\,\text{erg s}^{-1}$ increases by about 1 dex from $z = 0$ to $z \approx 1-2$. Although the origin of this trend is unclear, it can be interpreted as an enhancement of the average star formation rate in lower-luminosity AGN at $z \approx 2$ compared to the local Universe. In this picture, the enhanced star formation is likely to have an impact on the mid-IR part of the SED and will make lower-luminosity AGN at $z \approx 1-2$ appear underluminous at X-rays for their mid-IR luminosity compared to local AGN samples. This would be in agreement with our interpretation of the IRX population and emphasizes the need to properly model the mid-IR part of the SED to assess the relative contribution of AGN and star formation at this wavelength regime.

Further progress in the study of IRX galaxies is expected from upcoming Herschel observations, which when combined with the existing *Spitzer* data will constrain the SEDs of individual sources at $z \approx 2$ over a sufficiently large wavelength baseline (mid- to far-IR) to allow decomposition of the AGN and starbursts components through template fits, as done in this paper. This exercise will provide estimates of the level of dusty star formation activity and the intrinsic AGN luminosity of individual sources to confirm or refute claims that they are Compton thick QSOs. The determination of the column density of these sources through X-ray spectroscopy has to wait future X-ray missions with large collecting areas, such IXO, which is expected to provide spectra for $z \approx 2$ IRX sources which have typical X-ray fluxes $f_X(2-10\,\text{keV}) \approx 10^{-17}\,\text{erg s}^{-1}\,\text{cm}^{-2}$ (Georgantopoulos et al. 2009) and are currently accessible only through stacking analysis.

ACKNOWLEDGMENTS

REFERENCES

Akylas A., Georgantopoulos I., Georgakakis A., Kitsionas S., Hatzimi-naoglou E., 2006, A&A, 459, 693
Alonso-Herrero A. et al., 2006, ApJ, 640, 167
Babbedge T. S. R. et al., 2004, MNRAS, 353, 654
Barger A. J. et al., 2003, AJ, 126, 632
Barger A. J., Cowie L. L., Mushotzky R. F., Yang Y., Wang W.-H., Steffen A. T., Capak P., 2005, AJ, 129, 578
Barmby P., Huang J., Ashby M. L. N., Eisenhardt P. R. M., Fazio G. G., Willner S. P., Wright E. L., 2008, ApJS, 177, 431
Brodwin M. et al., 2008, ApJ, 687, L65
Bauer F. E., Yan L., Sajina A., Alexander D. M., 2010, AJ, 710, 212
Broos P., Townsley L., Getman K., Bauer F., 2002, ACIS Extract, An ACIS Point Source Extraction Package. Pennsylvania State University
Brusa M. et al., 2005, A&A, 432, 69
Bussmann R. S. et al., 2009a, ApJ, 693, 750
Bussmann R. S. et al., 2009b, ApJ, 705, 184
Capak P. et al., 2004, AJ, 127, 180
Coil A. L., Newman J. A., Kaiser N., Davis M., Ma C., Kocevski D. D., Koo D. C., 2004, ApJ, 617, 765
Cowie L. L., Barger A. J., Bautz M. W., Brandt W. N., Garmire G. P., 2003, ApJ, 584, L57
Daddi E. et al., 2007, ApJ, 670, 173
Davis M. et al., 2003, in Guhathakurta P., ed., Society of Photo-Optical Instrumentation Engineers (SPIE) Conference Series Vol. 4834, Science Objectives and Early Results of the DEEP2 Redshift Survey. SPIE, Bellingham, WA, p. 161
Davis M. et al., 2007, ApJ, 660, L1
Dey A. et al., 2008, ApJ, 677, 943
Donley J. L., Rieke G. H., Pérez-González P. G., Rigby J. R., Alonso-Herrero A., 2007, ApJ, 660, 167
Donley J. L., Rieke G. H., Pérez-González P. G., Barro G., 2008, ApJ, 687, 111
Draper A. R., Ballantyne D. R., 2009, ApJ, 707, 778
Efstathiou A., Rowan-Robinson M., 1995, MNRAS, 273, 649
Efstathiou A., Rowan-Robinson M., 2003, MNRAS, 343, 322
Efstathiou A., Rowan-Robinson M., Siebenmorgen R., 2000, MNRAS, 313, 734
Elvis M. et al., 1994, ApJS, 95, 1
Fiore F. et al., 2008, ApJ, 672, 94
Fiore F. et al., 2009, ApJ, 693, 447
Georgakakis A., Rowan-Robinson M., Babbedge T. S. R., Georgantopoulos I., 2007, MNRAS, 377, 203
Georgakakis A., Nandra K., Laird E. S., Aird J., Trichas M., 2008, MNRAS, 388, 1205
Georgakakis A. et al., 2009, MNRAS, 397, 623
Georgantopoulos I., Georgakakis A., Rowan-Robinson M., Rovilos E., 2008, A&A, 484, 671
Georgantopoulos I., Akylas A., Georgakakis A., Rowan-Robinson M., 2009, A&A, 507, 747
George I. M., Turner T. J., Netzer H., Nandra K., Mushotzky R. F., Yaqoob T., 1998, ApJS, 114, 73
Getman K. V. et al., 2005, ApJS, 160, 319
Ghisellini G., Haardt F., Matt G., 1994, MNRAS, 267, 743
Gilli R., Comastri A., Hasinger G., 2007, A&A, 463, 79
Gondek D., Zdziarski A. A., Johnson W. N., George I. M., McNaron-Brown K., Magdziarz P., Smith D., Gruber D. E., 1996, MNRAS, 282, 646
Hatziminaoglou E. et al., 2005, AJ, 129, 1198
Hickox R. C., Markevitch M., 2006, ApJ, 645, 95
Ilbert O. et al., 2006, A&A, 457, 841
Lacy M. et al., 2004, ApJS, 154, 166
Laird E. S. et al., 2009, ApJS, 180, 102
Lutz D., Maiolino R., Spoon H. W. W., Moorwood A. F. M., 2004, A&A, 418, 465
Marshall F. E., Boldt E. A., Holt S. S., Miller R. B., Mushotzky R. F., Rose L. A., Rothschild R. E., Serlemitsos P. J., 1980, ApJ, 235, 4
Matt G. et al., 1999, A&A, 341, L39
Morrison R., McCammon D., 1983, ApJ, 270, 119
Mullaney J. R., Alexander D. M., Huynh M., Goulding A. D., Frayer D., 2009, MNRAS, 1649
Murphy E. J., Chary R., Alexander D. M., Dickinson M., Magnelli B., Morrison G., Pope A., Teplitz H. I., 2009, ApJ, 698, 1380
Nandra K., Pounds K. A., 1994, MNRAS, 268, 405
Nandra K. et al., 2007a, ApJ, 660, L11
Nandra K., O'Neill P. M., George I. M., Reeves J. N., 2007b, MNRAS, 382, 194
Narayanan D. et al., 2009, preprint (ArXiv0910.2234)
Pérez-González P. G. et al., 2005, ApJ, 630, 82

Pérez-González P. G. et al., 2008, ApJ, 675, 234

Polletta M. d. C., et al., 2006, ApJ, 642, 673

Pope A. et al., 2008, ApJ, 689, 127

Prieto M. A., Reunanen J., Tristram K. R. W., Neumayer N., Fernandez-Ontiveros J. A., Orienti M., Meisenheimer K., 2010, MNRAS, 402, 724

Ranalli P., Comastri A., Setti G., 2003, A&A, 399, 39

Risaliti G., Elvis M., 2004, in Barger A. J., ed., Supermassive Black Holes in the Distant Universe Vol. 308 of Astrophysics and Space Science Library, A Panchromatic View of AGN. p. 187

Rowan-Robinson M., 1995, MNRAS, 272, 737

Rowan-Robinson M. et al., 2005, AJ, 129, 1183

Rowan-Robinson M. et al., 2008, MNRAS, 386, 697

Rowan-Robinson M., Valtchanov I., Nandra K., 2009, MNRAS, 397, 1326

Sajina A. et al., 2008, ApJ, 683, 659

Sazonov S., Revnivtsev M., Krivonos R., Churazov E., Sunyaev R., 2007, A&A, 462, 57

Stern D. et al., 2005, ApJ, 631, 163

Sutherland W., Saunders W., 1992, MNRAS, 259, 413

Terashima Y. et al., 2002, ApJ, 139, 1

Townsley L. K., Feigelson E. D., Montmerle T., Broos P. S., Chu Y., Garmire G. P., 2003, ApJ, 593, 874

Tozzi P. et al., 2006, A&A, 451, 457

Treister E. et al., 2009a, ApJ, 706, 535

Treister E., Urry C. M., Virani S., 2009b, ApJ, 696, 110

Weiner B. J. et al., 2005, ApJ, 620, 595

Wirth G. D. et al., 2004, AJ, 127, 3121

Worsley M. A. et al., 2005, MNRAS, 357, 1281

Yan L. et al., 2007, ApJ, 658, 778

This paper has been typeset from a TEX/LATEX file prepared by the author.